# Crystallization of Highly Oriented ZnO Microrods on Carboxylic Acid-Terminated SAMs

R. Turgeman,[†] O. Gershevitz,[†] M. Deutsch,[‡] B. M. Ocko,[§] A. Gedanken,*[,†] and C. N. Sukenik[†]

*Department of Chemistry and Kanbar Laboratory for Nanomaterials at the Bar-Ilan University Center for Advanced Materials and Nanotechnology, Bar-Ilan University, Ramat-Gan, 52900, Israel, Departments of Physics, Bar-Ilan University, Ramat-Gan 52900, Israel, and Physics Department, Brookhaven National Laboratory, Upton, New York 11973*

*Received June 10, 2005. Revised Manuscript Received August 8, 2005*

Highly oriented microrods ZnO crystals having a narrow size distribution were successfully crystallized on Si wafers coated with $SiCl_3(CH_2)_{11}-O-C_6H_4-COOH$. The relationship between surface properties and the crystallization products was investigated by ellipsometry, wetting measurements, X-ray reflectivity (XR), and grazing incidence diffraction (GID). The influence of the phenyl ether chromophore and the carboxylic group were explored by comparing the crystallization products obtained on monolayers made from $SiCl_3(CH_2)_{11}-O-C_6H_4-COOCH_3$, $SiCl_3(CH_2)_{16}-COOH$, and $SiCl_3(CH_2)_{16}-COOCH_3$ molecules. The results demonstrate that the carboxylic acid end group is crucial for achieving a highly oriented growth.

## 1. Introduction

Being a wide band-gap semiconductor (3.3 eV at 300 K), ZnO has a diverse range of technological applications. ZnO is currently in use, or being considered for use, as a phosphor,[1] as a component in electro-optical devices,[2−8] as a piezoelectric transducer,[1,9,10] as varistors,[1,11,12] as UV and microwave absorbers,[1,10] as gas sensors,[1,13−15] and for making transparent conducting films.[1,16] In addition to its superior electronic and optical properties, it is a low-cost II−VI semiconductor that is environmentally friendly. ZnO has several fundamental advantages over its competitors (Si, GaAs, CdS, ZnSe, and GaN): (1) its exciton is bound with a binding energy of 60 meV, which is much higher than that of GaN (25 meV) and ZnSe (22 meV). It should be noted that in order to achieve efficient excitonic laser action at room temperature, the binding energy of the exciton must be larger than the thermal energy at room temperature (26 meV); (2) it allows wet chemical processing; and (3) it is more resistant to radiation damage, and thus should be useful for space applications.[17]

The physical properties of crystalline materials depend on their crystal morphology and habit, crystallite size, the content of impurities or dopants, and the presence of structural defects. ZnO is a polar crystal whose polar axis is the *c*-axis; its space group is $C_{6v} = P_63mc$.[18] The ZnO has a wurtzite crystal structure ($a = 3.25$ Å and $c = 5.206$ Å). Each $Zn^{2+}$ ion is surrounded by four $O^{2-}$ ions and vice versa. This structure can be described schematically as alternating planes of O and Zn ions stacked along the *c*-axis. The nonpolar planes are $(10\bar{1})$, $(11\bar{2})$, and the polar faces are (001), which is Zn-terminated, and $(00\bar{1})$, which is O-terminated.

The two polar ZnO faces are the most intriguing from both the fundamental and applied point of view. The nonpolar surfaces are formed by breaking the same number of oxygen and zinc bonds and they contain an equal number of O and Zn ions, whereas the polar surfaces are either Zn- or O-terminated. Although the differences in the properties of

* To whom correspondence should be addressed.
[†] Department of Chemistry and Kanbar Laboratory for Nanomaterials at the Bar-Ilan University Center for Advanced Materials and Nanotechnology, Bar-Ilan University.
[‡] Departments of Physics, Bar-Ilan University.
[§] Physics Department, Brookhaven National Laboratory.

(1) Look, D. C. *Mater. Sci. Eng. B* **2001**, *80*, 383−387.
(2) Chopra, K. L., Das, S. R., Eds. *Thin Film Solar Cells*; Plenum: New York, 1983.
(3) Karzel, H.; Potzel, W.; Kofferlein, M.; Schiessl, W.; Steiner, M.; Hiller, U.; Kalvius, G. M.; Mitchell, D. W.; Das, T. P.; Blaha, P.; Schwarz, K.; Pasternak, M. P. *Phys. Rev. B* **1996**, *53*, 11425−11438.
(4) Cho, S.; Ma, J.; Kim, Y.; Sun, Y.; Wong, G. K. L.; Ketterson, J. B. *Appl. Phys. Lett.* **1999**, *75*, 2761−2763.
(5) Kong, L. B.; Li, F.; Zhang, Y.; Yao, X. *J. Mater. Sci. Lett.* **1998**, *17*, 769−771.
(6) Shih, W. C.; Wu, M. S. *J. Cryst. Growth* **1994**, *137*, 319−325.
(7) Troy, C. T. *Photonics Spectra* **1997**, *31*, 34−34.
(8) Vanheusden, K.; Seager, C. H.; Warren, W. L.; Tallant, D. R.; Caruso, J.; Hampden Smith, M. J.; Kodas, T. T. *J. Lumin.* **1997**, *75*, 11−16.
(9) Bailar, J. C., Emele'us, H. J., Nyholm, R., Trotman-Dickenson, A. F., Eds. *Comprehensive Inorganic Chemistry*; Pergamon Press: Oxford, 1973.
(10) Hutson, A. R. *Phys. Rev. Lett.* **1960**, *4*, 505−507.
(11) Gupta, T. K. *J. Am. Ceram. Soc.* **1990**, *73*, 1817−1840.
(12) Lee, J.; Hwang, J. H.; Mashek, J. J.; Mason, T. O.; Miller, A. E.; Siegel, R. W. *J. Mater. Res.* **1995**, *10*, 2295−2300.
(13) Jin, Z. C.; Hamberg, I.; Granqvist, C. G.; Sernelius, B. E.; Berggren, K. F. *Thin Solid Films* **1988**, *164*, 381−386.
(14) Chatterjee, A. P.; Mitra, P.; Mukhopadhyay, A. K. *J. Mater. Sci.* **1999**, *34*, 4225−4231.
(15) Seiyama, T.; Kato, A.; Fujiishi, K.; Nagatani, M. *Anal. Chem.* **1962**, *34*, 1502−1503.
(16) Brett, M. J.; Parsons, R. R. *Solid State Commun.* **1985**, *54*, 603−606.
(17) (a) Look, D. C. *Mater. Sci. Eng. B* **2001**, *80*, 383−387 (b) Yang, P.; Yan, H.; Samuel, M.; Russo, R.; Johnson, J.; Saykally, R.; Morris, N.; Pham, J.; He, R.; Choi, H. J. *Adv. Funct. Mater.* **2002**, *12*, 323−331.
(18) Wyckoff, R. W. G. *Crystal Structures*, 2nd ed.; Interscience: New York, 1963−1971; Vol. 1, p 111.

10.1021/cm051234q CCC: $30.25 
Published on Web 09/03/2005

the Zn- and O-terminated faces have been reported in the literature, we will briefly describe here some of the phenomena resulting from these differences. Photoluminescence (PL) measurements from these two faces reveal a striking difference. Two dominant transitions are observed in PL from the O face and barely any PL is observed from the Zn face.[19] Measurements of cathode luminescence and scanning tunneling spectroscopy of ZnO single crystals show that both surface electrical properties and luminescent characteristics depend on the face studied.[20] Polar O-terminated surfaces show an intrinsic conduction behavior with a surface band gap ranging from 0.4 to 0.8 eV. Zn-terminated surfaces show mainly n-type conduction. The nonpolar faces present either intrinsic or p-type behavior.[20] Feng et al. found that aligned ZnO nanorod films show reversible behavior from super-hydrophobicity to super-hydrophilicity.[21] This reversible behavior can be controlled by alternation of UV illumination and dark storage. The polar ZnO surfaces constitute a large fraction in high surface area powder samples and have been reported to be active crystal planes in methanol synthesis.[22]

Crystallization of highly aligned ZnO films can be achieved by vapor-phase transport,[23,24] sol−gel methods,[24−26] hydrothermal growth,[27,28] melt growth,[29] chemical vapor deposition (MOCVD),[30] electrochemical deposition,[31−34] laser ablation,[35] sputtering,[36] molecular beam epitaxy[37,38] and spraying arc-discharge.[39] However, large-scale use will require the development of simple, low-cost approaches. One such method is to grow ZnO crystals from aqueous solution at temperatures below 100 °C. The feasibility of ZnO crystal engineering under mild conditions was demonstrated by use of surfactants,[40−42] crystallization additives,[43] and polymers[44,45] and by crystal growth on Langmuir monolayers[46] and self-assembled monolayers (SAM).[47a,47b]

One of the most commonly used methods for growing ZnO crystals under mild conditions is the hydrolysis of a zinc nitrate solution. The hydrolysis is typically done at 95 °C in the presence of hexamethylene tetra amine (HMT). We have used this method for growing ZnO crystals on various surfaces and particles.[47−49] ZnO crystals grown on silicon wafers coated with a monolayer of $SiCl_3(CH_2)_{11}-O-C_6H_5$ molecules[47] provided perpendicular, well-formed, organized ZnO crystals where the thickness of the $SiCl_3(CH_2)_{11}-O-C_6H_5$ monolayer was 1.4−1.6 nm. This type of surface has two important properties that are essential for the formation of oriented ZnO crystals. The first property is related to the order of SAMs and the second property is related to the flexibility of the dipolar functional group. We have proposed that the mild molecular dipole (1−2 D) of the phenyl ether chromophore, when properly organized at the surface of the monolayer film, is crucial to the formation of preferentially oriented ZnO crystals.

Having shown that monolayer-covered surfaces can influence the orientation of ZnO crystal growth, as a function of the monolayer's nature and organization, we explore herein the influence of monolayers incorporation phenyl-ether groups bearing other functional groups on the structure of the monolayer-nucleated ZnO crystals. This work examined how this additional parameter can be used to influence both monolayer packing and crystal growth. We have chosen functional groups at the para position of the aromatic ring, which should provide a larger dipole moment relative to the $SiCl_3(CH_2)_{11}-O-C_6H_5$ . We have chosen the carboxylic acid as the functional group because it was reported in the literature that $-CO_2H$-rich surfaces interact strongly with growing ZnO.[50] Also, the acid/base properties of siloxane-


(19) Sherriff, R. E.; Reynolds, D. C.; Look, D. C.; Jogai, B.; Hoelscher, J. E.; Collins, T. C.; Cantwell, G.; Harsch, W. C. *J. Appl. Phys.* **2000**, *88*(6), 3454−3457.
(20) Urbieta, A.; Fernandez, P.; Hardalov, C.; Piqueras, J.; Sekiguchi, T. *Mater. Sci. Eng. B* **2002**, *91*−*92*, 345−348.
(21) Feng, X.; Feng, L.; Jin, M.; Zhai. J.; Jiang, L.; Zhu, D. *J. Am. Chem. Soc.* **2004**, *126*, 62−63.
(22) Bowker, M.; Honghton, H.; Wangh, K. C.; Giddings. T.; Green, M. *J. Catal.* **1983**, *84*, 252−255.
(23) Look, D. C.; Reynolds, D. C.; Sizelove, J. R.; Jones, R. L.; Litton, C. W.; Cantwell, G.; Harsch, W. C. *Solid State Commun.* **1998**, *105*, 399−401.
(24) Takahashi, N.; Kaiya, K.; Omichi, K.; Nakamura, T.; Okamoto, S.; Yamamoto, H. *J. Cryst. Growth* **2000**, *209*, 822−827.
(25) Spanhel, L.; Anderson, M. A. *J. Am. Chem. Soc.* **1991**, *113*, 2826−2833.
(26) Carnes, C. L.; Klabunde, K. J. *Langmuir* **2000**, *16*, 3764−3772.
(27) Suscavage, M.; Harris, M.; Bliss, D.; Yip, P.; Wang, S. Q.; Schwall, D.; Bouthillette, L.; Bailey, J.; Callahan, M.; Look, D. C.; Reynolds, D. C.; Jones, R. L.; Litton, C. W. *MRS Internet J. Nitride Semicond. Res.* **1999**, *4*, G 3.40, Suppl. 1.
(28) Kortounova, E. V.; Lyutin, V. I. *Ann. Chim. Sci. Mat.* **1997**, *22*, 647−650.
(29) Nause, J. *III*−*Vs Review*. **1999**, *12*, 28−31.
(30) Kim, J. S.; Marzouk, H. A.; Reucroft, P. J.; Hamrin, C. E. *Thin Solid Films* **1992**, *217*, 133−137.
(31) Masanobu, I.; Takashi, O. *Appl. Phys. Lett.* **1996**, *68*, 2439−2440.
(32) Peulon, S.; Lincot, D. *J. Electrochem. Soc.* **1998**, *145*, 864−874.
(33) Yoshida, T.; Tochimoto, M.; Schlettwein, D.; Wohrle, D.; Sugiura, T.; Minoura, H. *Chem. Mater.* **1999**, *11*, 2657−2667.
(34) O'Regan, B.; Schwartz, D. T.; Zakeeruddin, S. M.; Gratzel, M. *Adv. Mater.* **2000**, *12*, 1263−1267.
(35) Ardakani, H. K. *Thin Solid Films* **1996**, *287*, 280−283.
(36) Valentini, A.; Quaranta, F.; Penza, M.; Rizzi, F. R. *J. Appl. Phys.* **1993**, *73*, 1143−1145.
(37) Chen, Y. F.; Bagnall, D. M.; Koh, H. J.; Park, K. T.; Hiraga, K.; Zhu, Z. Q.; Yao, T. *J. Appl. Phys.* **1998**, *84*, 3912−3918.
(38) Chen, Y. F.; Bagnall, D. M.; Zhu, Z. Q.; Sekiuchi, T.; Park, K. T.; Hiraga, K.; Yao, T.; Koyama, S.; Shen, M. Y.; Goto, T. *J. Cryst. Growth* **1997**, *181*, 165−169.
(39) Kitano, M.; Hamabe, T.; Maede, S. *J. Cryst. Growth* **1993**, *128*, 1099−1103.
(40) Guo, L.; Ji, L. Y.; Xu, H. *J. Am. Chem. Soc.* **2002**, *124*, 14864−14865.
(41) Tian, Z. R.; Voigt, J. A.; McKenzie, B.; McDermott, J. M. *J. Am. Chem. Soc.* **2002**, *124*, 12954−12955.
(42) Choi, K. S.; Lichtenegger, H. C.; Stucky, G. D. *J. Am. Chem. Soc.* **2002**, *124*, 12402−12403.
(43) Taubert, A.; Wegner, G. *J. Mater. Chem.* **2002**, *12*, 805−807.
(44) Kumar, R. V.; Elgamiel, R.; Koltypin, Y.; Norwig, J.; Gedanken, A. *J. Cryst. Growth* **2003**, *250*, 409−417.
(45) Öner, M.; Norwig, J.; Meyer, W. H.; Wegner, G. *Chem. Mater.* **1998**, *10*, 460−463.
(46) (a) Weissbuch, I.; Addadi, L.; Berkovitch-Yellin, Z.; Gati, E.; Lahav, M.; Leiserowitz, L. *J. Am. Chem. Soc.* **1983**, *105*, 6613. (b) Landau, M.; Levanon, M.; Lahav, M.; Leiserowitz, L.; Sagiv, J. *Nature* **1985**, *318*, 353. (c) Grayer Wolf, S.; Leiserowitz, L.; Lahav, M.; Deutsch, M.; Kjaer, K.; Als-Nielson, J. *Nature* **1987**, *328*, 63. (d) Landau, M.; Popovitz-Biro, R.; Levanon, M.; Leiserowitz, L.; Lahav, M. *Mol. Liq. Cryst.* **1986**, *134*, 323. (e) Kuzemenko, I.; Rapaport, H.; Kajaer, K.; Als-Nielsen, J.; Weissbuch, I.; Lahav, M.; Leiserowitz, L. *Chem. Rev.* **2001**, *101*, 1659−1696.
(47) (a) Turgeman, R.; Gershevitz, O.; Palchik, O.; Deutsch, M.; Ocko, B. M.; Gedanken, A.; Sukenik, C. N. *Cryst. Growth Des.* **2004**, *4*, 169−175. (b) De Guire, M. R.; Niesen, T. P.; Supothina, S.; Wolff, J.; Bill, J.; Sukenik, C. N.; Aldinger, F.; Heuer, A. H.; Ruhle, M. *Z. Metallkd.* **1998**, *89*, 758−766. (c) Tidswell, I. M.; Ocko, B. M.; Pershan, P. S.; Wasserman, S. R.; Whitesides, G. M.; Axe, J. D. *Phys. Rev. B* **1990**, *41*, 1111−1128.
(48) Turgeman, R.; Tirosh, S.; Gedanken, A. *Chem. Eur. J.* **2004**, *10*, 1845−1850.
(49) Turgeman, R.; Gedanken, A. Submitted to *Cryst. Growth Des.*

anchored COOH-terminated SAMs have been investigated[51] both for a carboxylic acid-bearing alkyl chain, $SiCl_3-(CH_2)_{16}-COOH$ and for a carboxylic acid-functionalized phenolate ring, $SiCl_3(CH_2)_{11}-O-C_6H_4-COOH$. Two $pK_a$ values were observed in both cases ($pK_a$ values of $4.9 \pm 0.4$ and $9.3 \pm 0.2$ for the alkyl chain and $pK_a$ values of $4.7 \pm 0.3$ and $9.0 \pm 0.3$ for the benzoic acid). The percentage of material ionized at the first $pK_a$ was ~50% for the alkyl chain and ~70% for the benzoic acid at the pH values that are relevant to our ZnO crystallization process, i.e., 5−6. We explore the organization and the order of these acid-functionalized films by X-ray reflectivity (XR) and grazing-incidence diffraction (GID) measurements using synchrotron radiation.

Our strategy for exploring the influence of the surface carboxylic acid moieties on ZnO crystallization involved comparing results obtained from crystallization of ZnO on silicon wafers coated with $SiCl_3(CH_2)_{11}-O-C_6H_4-COOH$, denoted by BA for benzoic acid and those which were coated with $SiCl_3(CH_2)_{11}-O-C_6H_4-COOCH_3$, denoted by BE for benzoic ester. Investigation of the influence of the aromatic ring involved comparing these results with those obtained from ZnO crystallization on silicon wafers coated with $SiCl_3-(CH_2)_{16}-COOH$, denoted as AA for alkyl acid and with $SiCl_3(CH_2)_{16}-COOCH_3$, denoted by AE for alkyl ester.

## 2. Experimental Section

**a. Preparation of the Monolayers.** Although SAM deposition and characterization is reported in the literature,[51] we will mention here briefly some details. SAMs were created using a 0.012 mM solution of either benzoyl or alkyl ester-trichlorosilane in dicyclohexane, using the reported surface preparation procedures (cleaning and activation of the silicon wafers) and deposition conditions. Ester-functionalized SAM-coated wafers were placed in an oven-dried 150 mL flat-bottom flask, equipped with a small magnetic stirring bar and a reflux condenser, and maintained under a nitrogen atmosphere. Dry $CH_3CN$ (60 mL) and $AlI_3$ (1 g) was added to the flask. The reaction was heated at reflux (85 °C) for 2 h with extensive stirring. After cooling the reaction solution to room temperature, the substrate was rinsed with fresh $CH_3CN$ and then with distilled water and placed in 10% HCl for 1 h in order to remove aluminum salts. The resulting modified wafer with acid surface functional groups was then rinsed with water, sonicated in ethanol for 10 min, and dried with a stream of nitrogen.

**b. Characterization of the Monolayer.** *(1) Contact Angle and Ellipsometry.* Advancing and receding contact angle measurements of the coated silicon wafers were conducted under ambient conditions using a Rame-Hart NRL goniometer. All samples were measured at least three times. Contact angle measurements were done before and after the in situ transformation of ester- to carboxylic acid-functionalized monolayer and showed the expected decrease in both advancing and receding contact angle upon conversion of ester into acid. The values were identical to those reported in ref 51.

The film thickness on the Si wafers was measured by a spectrometric ellipsometer (Model M44 - J.A WOOLLAM Co.) using 44 wavelengths between 680 and 1108 nm. Analysis employed the VASE software provided with the ellipsometer. The ellipsometrically determined thickness was compared to a theoretical thickness value estimated from the length of the fully extended chain of the SAM-forming molecule, calculated using PCMODEL (Serena Software).

*(2) IR Spectroscopy.* ATR-FTIR data were obtained using a Bruker Vector 22 spectrometer. Spectra of the as-deposited films were collected using a $60 \times 20 \times 0.45$ mm Si parallelogram prism, prepared in-house by polishing the two short edges of a freshly cut double-side polished silicon wafer to a 45° angle. The background data were collected after the piranha treatment of the cleaned ATR prism, and the sample data were collected after the deposition of the monolayer. The background spectrum of the clean ATR prism was subtracted from each sample spectra. Typically, 44 sample scans were collected, at a nominal resolution of 4 $cm^{-1}$.

*(3) Surface Specific X-ray Measurements.* The synchrotron X-ray measurements were carried out using a conventional 6-circle diffractometer at beamline X22A, National Synchrotron Light Source, Brookhaven National Laboratory, at a wavelength of $\lambda = 1.155$ Å. The samples were placed in a sealed cell, having Kapton X-ray windows. A flow of oxygen-free helium through the cell reduced parasitic scattering and minimized beam damage to the sample.

The X-ray methods are described in detail in the literature[47a,c] and will be described here only briefly. Two types of measurement were carried out: X-ray reflectivity, (XR), where the fraction of the incident intensity reflected specularly, $R(q_z)$, is measured as a function of the surface-normal wave vector transfer, $q_z = (4\pi/\lambda)\sin\alpha$, where $\alpha$ is the incidence angle. XR yields information on the surface-normal structure of the monolayer such as the surface-normal electron density profile, the layer thickness, and the surface roughness. These quantities can be extracted from $R(q_z)$ by a standard procedure where a model is assumed for the density profile, the corresponding reflectivity is calculated from this model, and the parameters defining the model are obtained by computer-fitting the calculated reflectivity curve to the measured $R(q_z)$.

The in-plane order is studied by grazing incidence diffraction (GID). Here, the incidence angle is kept at $\alpha < \alpha_c$, where $\alpha_c$ is the critical angle for total external reflection, and the diffracted intensity is measured vs the surface parallel wave vector transfer $q_{||} = (4\pi/\lambda)\sin(\theta)$, where $2\theta$ is the surface-parallel angular offset of the detector from the reflection plane. The angular positions of the Bragg peaks, $q_{||}$, in the GID pattern yield the repeat distances $d = 2\pi/q_{||}$ for the 2-D lattice structure of the monolayer. For the hexagonal packing found here, the intermolecular distance is given by $D = d/\cos 30°$, the area per molecule in the surface plane is $A = d \times D$, and the molecular area in the plane perpendicular to the molecular long axis $-A_\perp = A \times \cos(\varphi)$, where $\varphi$ is the tilt angle of the molecule from the vertical in one of the symmetry directions. The two-dimensional Debye−Scherrer equation, $\xi = (0.9 \times 2\pi)/\Delta q_{||}$, allows us to extract the crystalline coherence length $\xi$ within the monolayer from the fwhm (full-width at the half-maximum), $\Delta q_{||}$, of a GID peak.

**c. Crystallization.** ZnO crystallization was done by hydrolyzing zinc nitrate solutions ($Zn(NO_3)_2 \cdot 6H_2O$, Aldrich) in the presence of HMT at 95 °C. The high temperature was chosen to prevent the formation of zinc hydroxide and afford the decomposition of HMT to ammonia and formaldehyde. This causes a shift of the pH of the solution from 5 to around 6, which is enough to cause the solubility product of ZnO to be exceeded. The SAM-coated silicon wafers were inserted into a Teflon holder. The Teflon holder was put inside the supersaturated solution on a glass ring with the wafer's coated surface facing downward to avoid ZnO crystals aggregating adventitiously on the surface. To minimize the effects

(50) Wegner, G.; Baum, P.; Muller, M.; Norwig, J.; Landfester, K. *Macromol. Symp.* **2001**, *175*, 349−355.
(51) Gershevitz, O.; Sukenik. C. N. *J. Am. Chem. Soc.* **2004**, *126*, 482−483.

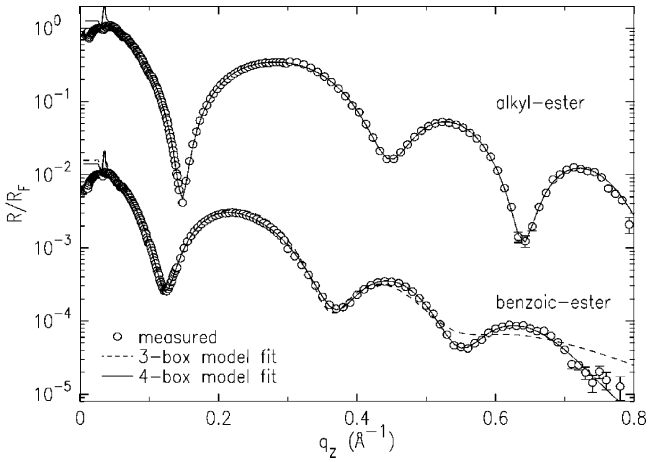


**Figure 1.** Fresnel-normalized measured (open circles) X-ray reflectivity curves for Si wafers coated with the indicated monolayers. Fits to the 3-box (dashed line) and 4-box (solid line) models, discussed in the text, are also shown. The corresponding electron density profiles are shown in Figure 2. Curves are shifted by 2 decades for clarity.

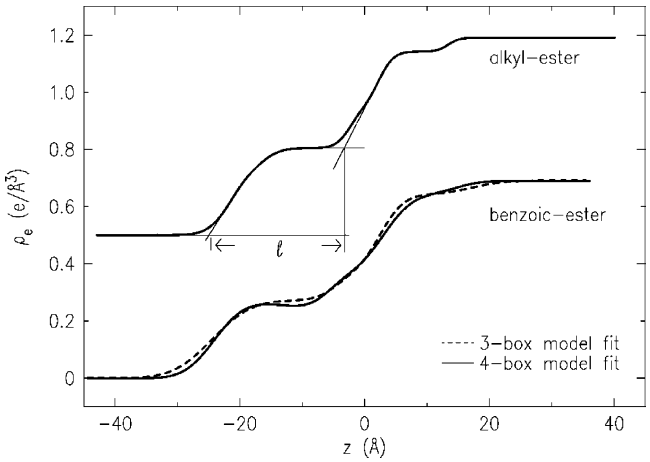


**Figure 2.** Surface normal density profiles derived from the 3-box and 4-box model fits to the measured X-ray reflectivity curves shown in Figure 1. The geometric construction whereby the monolayer's thickness is derived from the density profile is shown on the upper curve and is discussed in the text. Curves are shifted by 0.5 e/Å$^3$ for clarity.

of local variations in temperature, supersaturation, pH value, and stirring, several wafers were coated simultaneously. Each coating batch contained the four different functionalized alkyl silane SAMs: BE, BA, AE, and AA. To study the importance of precomplexation of zinc ions to the carboxylic acid surface, we grew ZnO crystals on SAMs by mixing together equal volumes of 0.03 M aqueous solutions of zinc nitrate and HMT in different sequences. One set of experiments (Procedure #1) was done by exposing the surface first to zinc nitrate solution and then to HMT solution. A second set of experiments (Procedure #2) was done by exposing the surface first to HMT and then to zinc nitrate solution. All the solutions were mixed at 95 °C.

**d. Crystal Characterization Methods.** The crystals were characterized by scanning electron microscope (SEM) measurements (JEOL-JSM 840 scanning electron microscope) and X-ray powder diffraction (Bruker AXS D* Advance Powder X-ray diffractometer, using Cu K$\alpha$ = 1.5418 Å radiation).

Crystal density and orientation were measured at three randomly chosen regions for each surface. The area of the SEM-analyzed surfaces was 16 $\mu$m$^2$. For determining the growth orientation in each picture, we counted the total number of ZnO crystals as well as the number of crystals with a perpendicular orientation. The results are presented as percentage of oriented crystals out of the total number of ZnO crystals. As defined previously,[47] samples exhibiting more than 50% oriented crystals are considered as showing oriented growth.

For measuring crystal width and length, three randomly chosen regions for each surface were analyzed. A population of at least 25 crystals in each region was used for each surface. SEM pictures were taken while the samples were aligned perpendicular and parallel to the beam.

## 3. Results and Discussion

**a. Monolayer Characterization.** The measured XR curves, normalized to the Frsenel reflectivity of an ideally flat and smooth surface of zero width, are shown in Figure 1 for wafers coated by a monolayer of benzoic ester (BE) and alkyl ester (AE). The sharp dips, particularly for AE, indicate a densely packed and uniform monolayer. An approximate value for the monolayer thickness, $l_a$, can be obtained from $l_a = \sqrt{\pi/((q_z^m)^2-(q_c)^2)}$, where $q_z^m$ and $q_c$ are the $q_z$-positions of the first minimum of the XR curve and the critical wavevector for total external reflection, respectively, with $q_c = 0.032$ Å$^{-1}$ for all our measurements. This equation yields for AE, where $q_z^m = 0.148$ Å$^{-1}$, a thickness of $l_a = 21.5$ Å, which as we show below coincides with the value derived from the full-XR-curve modeling. For BE, where $q_z^m = 0.124$ Å$^{-1}$, this approximation yields $l_a = 25.3$ Å, which overestimates the full-curve-fit value by about 7% (see below). One should note, however, that the equation above for $l_a$ is valid only for a uniform-density layer on top of a uniform-density substrate. For our samples, the nonuniform periods of the Kiessig fringes in Figure 1 indicate that the density profile cannot be characterized by a single-length scale only; i.e., it cannot be described simply by a single-density monolayer on top of a single-density substrate. Thus, the approximation above may not be reliable, and a full-curve fit of the measured XR curves is required to obtain the monolayer's thickness.

For the full-curve fits we employ the so-called "box model", consisting of a number $n$ of slabs, each of a (constant) density $\rho_i$, width $w_i$, and interfacial width $\sigma_i$, to describe the surface-normal electron density profile. As discussed in detail in ref 47a and c, the reflectivity curve calculated analytically from the model for a chosen $n$ was least-squares-fitted to the measured reflectivity curve, yielding the best-fit values for $\rho_i$, $w_i$, and $\sigma_i$. These fit-generated parameters are used to plot the density profile. The profiles corresponding to the XR curves in Figure 1 are shown in Figure 2. The smallest number of slabs which provides a good fit to the measured XR curves over the full $q_z$ range measured was $n = 4$. As demonstrated by the XR curves in Figure 1, the 4-box model provides an excellent fit to both measured curves. The best 3-box fit deviates significantly from the measured XR for $q_z \geq 0.5$ Å$^{-1}$. Nevertheless, the electron density profile obtained even from this imperfect fit (dashed line in Figure 2) is very close to that derived from the 4-box model, indicating the robustness of the density profile derived from the fits.

The profiles show the high-density Si substrate on the right-hand, positive-$z$ side of Figure 2, and the lower-density monolayer of the left-hand, negative-$z$ side of the figure, with

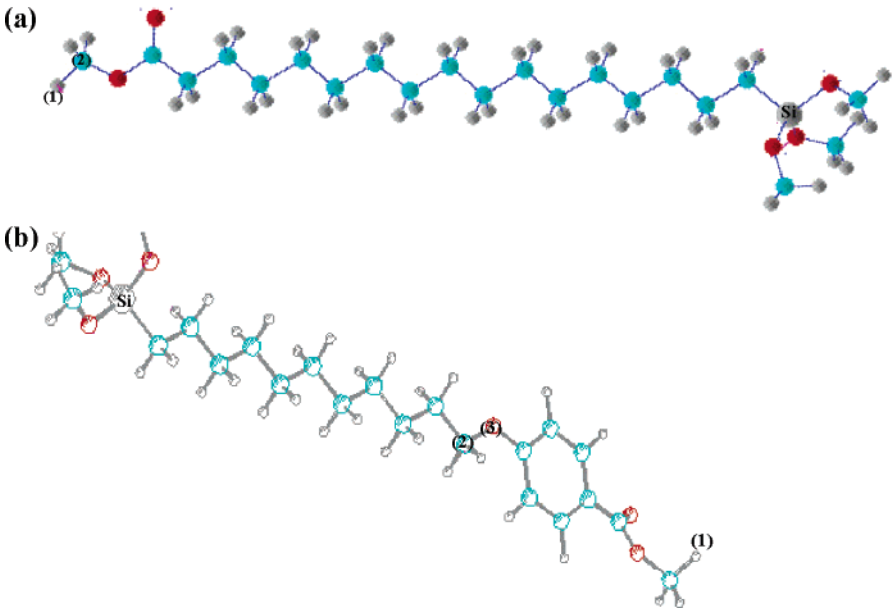


**Figure 3.** Molecular configurations for AE (a) and BE (b). In part (a) atom (1) indicates the topmost hydrogen atom of the terminal methyl and atom (2) indicates the carbon atom of the first methylene. In part (b) atom (1) indicates the topmost hydrogen atom of the terminal methyl ester and atoms (2) and (3) indicate the C−O bond which is bonded to the benzene ring.

a layer of slightly smaller density (presumably a native $SiO_2$) and a high-slope (rough) transition layer separating the two. A small bump, only a few Å wide, just below $z = 0$, and having a density slightly higher than that of the alkyl chains of the monolayer, is also observed. This is assigned to the layer of oxygen and silicon atoms of the silane headgroups, which bind the monolayer's molecules to the substrate.

The monolayer thickness, $l$, is derived from the density profiles by the geometrical construction depicted for the AE curve in Figure 2 and discussed in ref 47a and c. This yields thicknesses of $l = 21.7$ and 23.5 Å for the AE and BE, respectively.

For the AE, this value coincides with that derived above from the approximate formula of a simple monolayer, but for the BE the full-curve fit provides a thickness ~1.5 Å smaller than that of the approximate formula. This is not surprising in view of the deviation of the complex density profile obtained from the fit from the simple model assumed in deriving the approximate formula.

The thickness values derived from the XR fits can be better understood in the context of the molecular conformation, shown in Figure 3, as optimized by energy calculations, using the PC-model (Serena Software) program. Figure 3a illustrates the molecular conformation of the AE. The extended length of the AE molecule, measured from the near-substrate Si, to the topmost H of the terminal methyl (marked in Figure 3 as atom 1) is $l_{Si-H} = 25.1$ Å, while that from the carbon of the first methylene (marked in Figure 3 as atom 2) is $l_{C-H} = 23.6$ Å. With use of the XR-derived thickness, 21.7 Å, these yield average molecular tilts of 30° and 23°, respectively. We conclude therefore that the XR indicates a tilt of order (27 ± 4)° for the AE molecules comprising the monolayer. We also conducted in situ ATR-IR (attenuated total reflection infrared) measurements for AE, indicating a tilt angle of 24 ± 1°, in agreement with the XR results.

The density profile in Figure 2 for the BE molecule exhibits a slightly higher density toward the end of the molecule, where the benzene ring resides, as compared to the alkane chain part of the molecule. This is consistent with the expected higher packing of these individual segments. The fully optimized BE molecule yields $l_{Si-H} = 22.4$ Å, which is shorter than the length derived from the XR above. The main reason for this rather short length is a tilt of the axis of the benzyl-ester moiety away from that of the alkyl chain by 108°. Locking the C−O bond angle at 124.4° in the optimization process yields the conformation shown in Figure 3b, which has a smaller tilt, and a larger length: $l_{Si-H} = 23.4$ Å. This value is within ~0.3 Å of the value derived above from the XR fits. These values seem to indicate that the conformation of the BE molecules within the close-packed monolayer are probably more linear and extended than the conformation obtained from calculations for a single, stand-alone, molecule. Moreover, the molecular tilt for this layer has to be small as well, ≤10°, since the layer thickness is so close to the extended length. These conclusions are supported by the GID measurements discussed below. We also conducted in situ ATR-IR (attenuated total reflection infrared) measurements on BE, which indicated a tilt angle of 21 ± 1°. Since this tilt angle differs considerably from the XR results, additional measurements are needed for an exact determination of the tilt angle.

XR and GID measurements were not carried out for the other two molecules, AA and BA, addressed in this study by other methods. The reason for this is their high surface free energy and ease of contamination even at ultrahigh vacuum conditions, causing deterioration of the surface during the measurement.

The GID patterns measured for the same monolayer-coated Si wafers used in the XR measurements are shown in Figure 4. Only a single peak is observed, indicating a hexagonal packing of the molecules for both monolayers. The AE monolayer exhibits a broad peak, while that of BE consists of a relatively sharp peak on top of a broad one. The peaks were fitted by Gaussians, and the corresponding parameters

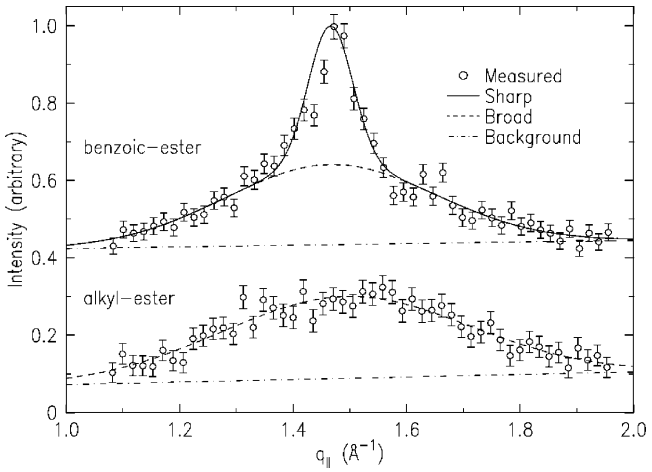


**Figure 4.** Grazing-incidence diffraction patterns for the sample indicated, the XR curves of which are shown in Figure 1. The in-plane structure of the monolayer, giving rise to these patterns, is discussed in the text. The curves are shifted by 0.4 for clarity.

**Table 1. Parameters Derived from the Fits of the GID Peaks in Figure 4**[a]

| sample | position (Å$^{-1}$) | width (Å$^{-1}$) | $d$ (Å) | $d$ (Å) | $A$ (Å$^2$) | $\xi$ (Å) |
|---|---|---|---|---|---|---|
| AE | 1.494 | 0.218 | 4.206 | 4.857 | 20.4 | 26 |
| BE(sharp) | 1.466 | 0.039 | 4.286 | 4.950 | 21.2 | 145 |
| BE(broad) | 1.466 | 0.185 | 4.286 | 4.950 | 21.2 | 31 |

[a] $d = 2\pi/q$ is the repeat distance giving rise to the GID peak at $q$, $D = d/\cos 30°$ is the corresponding molecular spacing, $A = d \times D$ is the area per molecule in the monolayer plane, and $\pi$ is the crystalline coherence length derived from the peak width.

derived from the peaks' positions and widths are summarized in Table 1.

The crystallinity of the AE monolayer is rather poor. The coherence length is short, ~5 molecular distances, only slightly larger than the 2−3 molecular distances in an amorphous solid or a liquid. The strong mutual dipolar repulsion of the molecules, due to the large dipole moment resulting from the ester moiety, may contribute to the short coherence length. The calculated dipole moments for the esters are as follows: BE = 4.13 D, AE = 4.25 D. We could not calculate the dipole moments of AA and BA because of problems in locking the hydrogen bonds. The BE monolayer exhibits two different types of ordered domains. One has roughly the same low crystalline coherence length as that of the AE film. However, the second component has a much higher crystallinity, with a coherence length of ~30 molecular distances.

The surface-plane molecular area of AE, $A = 20.4$ Å, corresponds to $A_\perp = 18.8$ Å in the plane perpendicular to the long molecular axis for the tilt angle of $\varphi = 23°$ deduced above. Within experimental uncertainties, this coincides with the molecular area of 18.7 Å$^2$ found for herringbone-structured surface-frozen monolayers of $C_{44}H_{50}$ alkane[52] and the 18.6 Å$^2$ of bulk alkanes[53] and of Langmuir films of alkyl derivatives.[54] The axis-normal molecular area of the untilted BE, 21.2 Å$^2$/molecule, is considerably larger. This is, however, not surprising in view of the bulkier benzyl moiety of the molecule. In fact, the $A_\perp = A$ of BE coincides with the 21.2 Å$^2$/molecule axis-normal molecular area measured for liquid-mercury-supported dense Langmuir film of MMB (4′-methyl-4-mercaptobiphenyl)[55] and the 21.6 Å$^2$/molecule found for the high-density $\epsilon$-phase of self-assembled monolayers of the same molecules on a solid Au substrate.[57] The molecular ordering in these two systems is also hexagonal, albeit with tilted molecules. Note also that the van der Waals cross-sectional area of the ring is 21.1 Å$^2$/molecule.[56] The fact that the molecular area of the BE almost coincides with this value indicates that the ring must be aligned with its plane roughly normal to the surface. Any other orientation will increase its surface-plane-projected area, and, consequently, also the area per molecule. Thus, the BE molecule should be extended and close to linear rather than the bent conformation discussed above. This supports the same conclusion obtained above based on the monolayer thickness derived from the model fit to the measured XR curve of BE.

**b. Comparison of the Crystallization of ZnO on Different Surfaces.** Detection of the growth of ZnO crystals with preferred orientation such that a particular crystal plane (*hkl*) is parallel to the substrate can be accomplished by XRD, when used in the α−α mode. In this mode the angles of incidence and detection are equal, both forming an angle α with the substrate, and thus, also with the (*hkl*) plane of interest. When crystal growth occurs only with substrate-parallel (*hkl*) planes, the XRD pattern will show all allowed orders of the (*hkl*) reflections, (*hkl*), (2*h*,2*k*,2*l*), (3*h*,3*k*,3*l*), etc. All other reflections, which originate in planes not parallel to (*hkl*), will be absent from the pattern. When the crystal growth is not exclusively in the preferred orientation, reflections due to non-(*hkl*)-parallel planes will also show up in the pattern.[57] The effective angular resolution of the XRD setup, which is determined by the angular divergence of the incident beam, and the angular acceptance of the detector, determines how large can be the misalignment of a particular Bragg plane from the plane of the substrate so that it is still picked up by the detector as a "surface-parallel" plane. This, in turn, will influence the fraction of the preferentially aligned crystallites out of the total, which will be deduced from an XRD pattern. The tighter the resolution, the smaller the fraction. The same fraction can be determined from SEM images, counting the oriented crystals by their apparent morphology. As orientational deviations from perfect alignment by up to a few degrees are difficult to resolve by eye, and since the resolution of an XRD instrument is usually significantly lower than this angular range, the XRD-determined fraction of preferentially oriented crystallites in a sample will usually be smaller than the same quantity determined from SEM images. Indeed, Whitesides et al. found that the percentages of oriented calcite crystals

(52) Ocko, B. M.; Wu, X. Z.; Sirota, E. B.; Sinha, S. K.; Gang, O.; Deutsch, M. *Phys Rev. E* **1997**, *55*, 3164.
(53) Kitaigorodskii, A. I. *Organic chemical crystallography*; Consultants Bureau: New York, 1961.
(54) Kaganer, V. M.; Mohwald, H.; Dutta, P. *Rev. Mod. Phys.* **1999**, *71*, 779.
(55) Tamam, L.; Kraack, H.; Sloutskin, E.; Ulman, A.; Pershan, P. S.; Ocko, B. M. *J. Phys. Chem B*, in press.
(56) (a) Leung, T. Y. B.; Schwartz, P.; Scoles, G.; Schreiber, F.; Ulman, A. *Surf. Sci.* **2000**, *458*, 34. (b) Azzam, W.; Fuxon, C.; Birkner, A.; Rong, H. T.; Buck, M.; Wöll, C. *Langmuir* **2003**, *19*, 4958.
(57) Klug, H. P.; Alexander, L. E. *X-ray Diffraction Procedures*; Wiley-Interscience: New York, 1974.

**Table 2. Observed Percentage of ZnO Crystals Oriented with Their {001} Plane Parallel to the Surface, as a Function of the Crystallization Conditions and the Functional Group[a]**

| sample | procedure #1 | procedure # 2 |
|---|---|---|
| AE (1) | 75 | 30 |
| AE (2) | 67 | 32 |
| BE (1) | 62 | 43 |
| BE (2) | 60 | 30 |
| AA (1) | 100 | 35 |
| AA (2) | 100 | 25 |
| BA (1) | 100 | 36 |
| BA (2) | 100 | 47 |

[a] ZnO crystallizations were done on two samples for each functional group (using each of the two procedures).

estimated using morphological analysis was higher than the values derived from the XRD spectra.[58]

Table 2 gives a comparison of crystallographic orientation of ZnO crystals, determined from SEM measurements, on four different surfaces when the nitrate solution is added first (procedure #1) and when the HMT is added first (procedure #2). The values in this table present the percentage of crystals oriented with their {001} plane parallel to the surface so that the long axis of these rod-shped crystallites is perpendicular to the substrate. To minimize the effects of local variations in temperature, supersaturation, pH value, and stirring, ZnO crystallization was done on all four different surfaces (AA, AE, BA, BE) simultaneously.

The crystallographic orientation of ZnO crystals was also investigated for the ester-terminated samples (AE and BE) that were prepared for the synchrotron X-ray measurements reported above. The ZnO crystals were grown on these surfaces using procedure #1. It should be noted that the monolayer-coated Si wafers used in the synchrotron measurements and those of Table 2 were prepared separately. The observed percentages of oriented crystals was 65% for AE and 61% for BE, both of which are in reasonable agreement with the range of values reported for the comparable experiments in Table 2.

It is clear that a better-oriented growth of ZnO crystals is achieved using procedure #1. This is true both for the ester surfaces and for the acid-terminated surfaces (AA and BA) where we always see 100% growth of crystals oriented along the ZnO *c*-axis under these conditions. Interestingly, samples of ZnO prepared using procedure #2 always show <50% oriented crystal growth, a result that we had previously defined as unoriented.[47] Thus, the sequence of reagent addition and the acid groups on the SAM surface emerge as the most important factors in orienting the ZnO growth.

Inspecting the ZnO structure shows that the {001} plane is perpendicular to the *c*-axis so that the preferred growth will proceed along the *c*-axis. It is expected, therefore, that growth along the *c*-axis will increase the length of the crystal faster than its width. This is indeed observed in the crystal dimensions and density of nucleation, as obtained from a statistical analysis on SEM images. These are summarized in Table 3.

Table 3 shows a general trend regarding the crystal size resulting from procedure #1 as compared with those grown by procedure #2. Crystals prepared by procedure #2 are shorter and narrower than those made by procedure #1. Also, the crystals grown on the acid-terminated surfaces are more monodispersed than those grown on the ester-terminated surfaces. This is manifested by the smaller standard deviation of the ZnO crystals grown on BA and AA surfaces as compared with those on AE and BE. It should also be noted that the BA SAMs surfaces provide the highest density of ZnO crystals (Figure 5).

The main results obtained from the above experiments are as follows:

(1) The best oriented growth is achieved when the SAMs surfaces are exposed to the zinc nitrate solution and afterward exposed to HMT solution.

(2) Growing ZnO crystal on acid-terminated SAMs surfaces induces 100% oriented crystal growth.

(3) Crystals grown on BA are 100% oriented and are very dense and monodisperse.

It is worth mentioning that in our previous paper[47a] we reported on the size and orientation growth of ZnO grown from a supersaturated solution without a SAM. The ZnO crystals of 3 $\mu$m length and 0.5 $\mu$m width did not show any oriented growth (see Figure 7a in ref 47a).

Our explanations for the absence of preferred orientation when the SAMs are exposed first to the HMT solution is related to the importance of zinc ion complexation controlling the face-selective nucleation. In accordance with the $pK_a$ of the acid surfaces, it is expected that with the addition of the HMT solution before the zinc nitrate solution the percentage of ionized material will increase. This will lead to a more polar surface and will be reflected in the density as well as the orientation of the ZnO crystals. In fact, we indeed obtain more ZnO crystals on the SAM surface, but these crystals are less well-oriented. The importance of zinc ion complexation for inducing ZnO crystallization is reported by O'Brien et al. in discussing the oriented growth of ZnO crystals grown from aqueous solutions containing zinc acetate and HMT on modified TO-glass surfaces.[59,60] The procedure for growing perpendicularly orientated ZnO rods involves two steps: modification of the TO-glass surfaces by CBD (chemical bath deposition) of a ZnO template layer (~500 nm), followed by subsequent growth of acicular rods on these templates. The role of acetate ions is 2-fold: (1) maintaining optimum solution pH and (2) serving as counterions by chemisorption to the ZnO *c*-planes. The choice of acetate ions as oriented growth promoters is based on recent reports by O'Brien suggesting adsorption of carboxylate ions on the polar planes of ZnO crystals. O'Brien concluded that a successful oriented growth of ZnO rods can be achieved by a combination of two factors: substrate effect and presence of counterions. We adopted O'Brien's approach in an opposite way. In his studies, the ZnO crystals were examined for their adsorption of ions while in our case the ZnO grew on SAMs terminated by a carboxylate group. The results

(58) Aizenberg, J.; Black, A. J.; Whitesides, G. M. *J. Am. Chem. Soc.* **1999**, *121*, 4500−4509.

(59) Boyle, D. S.; Govender, K.; O'Brien, P. *Chem. Commun*. **2002**, 80−82.

(60) Govender, K.; Boyle, D. S.; O'Brien, P.; Binks, D.; West, D.; Coleman, D. *Adv. Mater.* **2002**, *14*, 1221−

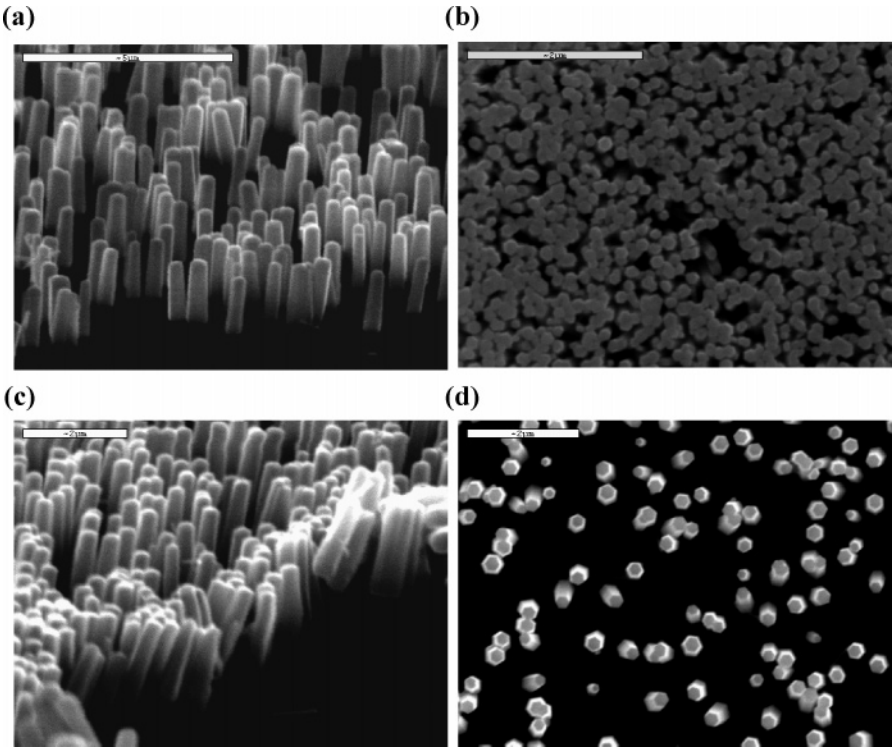


**Figure 5.** (a) and (b) are SEM images of ZnO crystals grown on silicon wafers coated with BA, $SiCl_3(CH_2)_{11}-O-C_6H_4-COOH$. (c) and (d) are SEM images of ZnO crystals grown on silicon wafers coated with AA, $SiCl_3-(CH_2)_{16}-COOH$. (a) and (d) were taken with the samples perpendicular to SEM beam. (c) and (d) are top side views taken while the samples were located parallel to the SEM beam. The crystals were grown using procedure #1.

**Table 3. General Results of ZnO Crystallization on Acid- and Ester-Terminated SAMs Obtained from SEM**

| | length ($\mu$m) | | width ($\mu$m) | | density of nucleation (crystal/$\mu m^2$) | |
|---|---|---|---|---|---|---|
| sample | procedure #1 | procedure #2 | procedure #1 | procedure #2 | procedure #1 | procedure #2 |
| AE (1) | $1.03 \pm 0.35$ | $0.57 \pm 0.07$ | $0.42 \pm 0.06$ | $0.15 \pm 0.03$ | $1.89 \pm 0.26$ | $2.72 \pm 0.82$ |
| AE (2) | $1.12 \pm 0.43$ | $0.51 \pm 0.12$ | $0.32 \pm 0.06$ | $0.19 \pm 0.03$ | $2.12 \pm 0.38$ | $2.98 \pm 0.36$ |
| BE (1) | $1.77 \pm 0.44$ | $0.44 \pm 0.08$ | $0.28 \pm 0.06$ | $0.16 \pm 0.03$ | $1.08 \pm 0.46$ | $9.96 \pm 2.12$ |
| BE (2) | $2.26 \pm 0.32$ | $0.51 \pm 0.12$ | $0.27 \pm 0.08$ | $0.14 \pm 0.04$ | $0.67 \pm 0.22$ | $3.26 \pm 1.78$ |
| AA (1) | $1.57 \pm 0.24$ | $0.45 \pm 0.09$ | $0.22 \pm 0.04$ | $0.15 \pm 0.04$ | $2.0 \pm 0.7$ | $12.09 \pm 1.34$ |
| AA (2) | $1.55 \pm 0.21$ | $0.45 \pm 0.08$ | $0.29 \pm 0.06$ | $0.14 \pm 0.02$ | $1.16 \pm 0.22$ | $3.39 \pm 0.62$ |
| BA (1) | $1.31 \pm 0.10$ | $0.47 \pm 0.12$ | $0.11 \pm 0.02$ | $0.16 \pm 0.03$ | $20.60 \pm 2.71$ | $6.56 \pm 2.23$ |
| BA (2) | $1.45 \pm 0.13$ | $0.41 \pm 0.09$ | $0.29 \pm 0.04$ | $0.12 \pm 0.03$ | $4.47 \pm 1.47$ | $11.02 \pm 3.99$ |

were similar in that the carboxylate accelerated the growth along the *c*-axis while avoiding the lateral growth.

The surface properties of the SAM are determined by a combination of its chain structure, the terminating functional group, and its dipole moment, and the packing and conformation of the monolayer. Obtaining 100% oriented crystals for BA and AA SAMs indicates the major role of the carboxylic acid and the minor effect of the other structural features in promoting oriented crystal growth. We attributed this result to the enhanced complexation of the zinc ions to terminal acid group. This would be expected to be greater than the complexation of the corresponding ester-terminated groups and would not be expected to vary much between the alkyl and benzoic acid surfaces. It is believed that the exposure of the SAM to the $Zn^{2+}$ ions enhances ordering of the surface, thus enabling a better oriented crystallization.

XR measurements which yield information about the surface-normal structure show that in the case of AE the tilt angle is $27 \pm 4°$, whereas the tilt angle for the benzyl-ester moiety is less than 10°. These findings concur with the GID measurements showing that the crystallinity of AE SAMs is relatively very poor as compared to the crystallinity of BE. XR and GID measurements show that the benzyl-ester ring must be aligned with its plane roughly normal to the surface. It seems that the benzene moiety does contribute to the increase in surface crystallinity and determines the molecular conformation. Combining the surface specific X-ray results, the calculated dipole moment values, with the crystallization results lead to the conclusion that the phenyl ether chromophore helps to align the dipole moments on the surface and create surfaces having a dense dipole moment profile. Thus, the function of the phenyl ether chromophore in the work reported herein is significantly different from the function attributed to it previously.[47] For SAMs of $SiCl_3-(CH_2)_{11}-O-C_6H_5$ the phenyl ether is the origin of the dipole moment, for the monolayers $SiCl_3(CH_2)_{11}-O-C_6H_4-COOH$ the phenyl ether is the agent directing the order and packing of the monolayer.

## Conclusion

The paper demonstrates that a denser and more uniformly oriented growth of ZnO crystals is achieved on films when the crystallization occurs on a carboxylic acid-bearing monolayer surface. The oriented growth is attributed to the

specific interaction that the carboxylate ions show toward the polar planes of the ZnO. This interaction is electrostatic and results from the high dipole moment of the carboxylate ion. The structural details of the monolayer bearing these acid groups most clearly influences the density of the ZnO crystals obtained.

**Acknowledgment.** The authors gratefully acknowledge support from the Germany-Israel Program (DIP) of the German DLR and from the GIF (German Israel Research Foundation) program. Beamtime at X22A, NSLS, is gratefully acknowledged. Brookhaven National Laboratory is supported by the U.S. Department of Energy under Contract DE-AC02-76CH00016.

**Supporting Information Available:** The XRD diffraction patterns of ZnO crystals grown on BA monolayers. This material is available free of charge via the Internet at http://pubs.acs.org.

CM051234Q